Available online at www.sciencedirect.com
SCIENCE DIRECT
Catalysis Today 116 (2006) 264–270
CATALYSIS TODAY
www.elsevier.com/locate/cattod

Improvement of activity and stability of Ni–Mg–Al catalysts by Cu addition during hydrogen production by catalytic decomposition of methane

A. Monzón [a,*], N. Latorre [a], T. Ubieto [a], C. Royo [a], E. Romeo [a], J.I. Villacampa [a], L. Dussault [b], J.C. Dupin [b], C. Guimon [b], M. Montioux [c]

[a] *Nanoscience Institute of Aragon (INA), University of Zaragoza, 50009 Zaragoza, Spain*
[b] *LCTPCM-UMR (CNRS) 5624 and FR 2606, 2 Avenue P. Angot, 64053 Pau Cedex 9, France*
[c] *CEMES, B.P. 94347, 31055 Toulouse Cedex 4, France*

Available online 13 July 2006

Abstract

Catalytic decomposition of methane is a potential alternative route for the production of hydrogen and carbon nanofilaments from natural gas and other feedstocks. In the present paper, we report the results of characterization and catalytic behaviour of Ni–Cu–Mg–Al catalysts.

The effect of the Cu addition in the catalyst composition on activity and stability has been investigated. The influence of operating temperature and feed composition on carbon content and carbon formation rate has also been studied. It has been shown that H_2 inhibits both the carbon filament formation and the encapsulation of metallic particles by coke. A higher reaction temperature increases both the deactivation rate and the growth rate of filaments. An increase in the methane concentration generates a rise of the rate of carbon filament formation.

The size of metal particles and the carbon filaments as well as the nanofilament texture depends on the copper content of the catalyst. When the Cu content is 7.6 wt.%, the carbon nanofilaments are nanofibers with a platelet texture, and the particles and CNFs sizes are widely distributed (50–400 nm).

Keywords: Catalytic methane decomposition; Hydrogen production; Carbon nanofibers; Platelet nanofibers; Ni–Cu catalysts

1. Introduction

Steam reforming of CH_4 (SRM) has been the most widely used and generally the most economical technology for the production of H_2 [1]. However, this route makes hydrogen an indirect source of CO_2. In addition, the co-product of SRM, CO, must be removed by two subsequent steps: water-gas shift and methanation. The complete removal of CO is not economical and therefore, the H_2 thus produced is not suitable for low-temperature fuel cells given that the catalyst is poisoned by CO [2]. The reaction of catalytic decomposition of methane (CDM) over nickel catalysts has recently been receiving attention as an alternative route to the production of H_2 from natural gas [1–6]. Furthermore, it has been proposed that the cracking route is superior to steam reforming from economical and energy efficiency points of view [2].

In addition to H_2, CDM produces carbon nanofibers or carbon nanotubes. These are valuable products that have been paid considerable attention in recent years owing to their excellent properties. In previous works [7], we obtained that the addition of MgO to $NiO–Al_2O_3$ catalysts, increases the catalyst activity. However, Ni–Mg–Al catalyst also suffers deactivation by coke formation at temperatures above 570 °C [7]. Moreover, it has been found that the Cu is able to enhance the activity of Ni–Al catalysts in this reaction [5], although the effect of this promoter on catalyst stability has not been studied. In this paper we present a study of the influence of the addition of Cu on the activity, and mainly

* Corresponding author.
E-mail address: amonzon@unizar.es (A. Monzón).

0920-5861/$ – see front matter © 2006 Elsevier B.V. All rights reserved.
doi:10.1016/j.cattod.2006.05.085

the stability of Ni–Mg–Al catalysts during the reaction of CDM.

2. Experimental

2.1. Materials

The catalysts, $NiO_x{\cdot}CuO_{1-x}{\cdot}MgAl_2O_4$ ($x = 1$, 0.8, 0.5 and 0.2), were prepared by coprecipitation of the metallic nitrates mixture at constant pH (10.2 ± 0.2) and temperature (60 °C). The corresponding mixed oxide was obtained by calcination of the dried hydrated precursor in N_2 at 800 °C for 11 h.

2.2. Characterization

Metallic content was determined by ICP-AES. The specific surface area of the mixed oxide was measured by adsorption of N_2 at 77 K with a Micromeritis Pulse Chemisorb 2700. The powder X-ray diffraction (XRD) pattern was recorded by an INEL diffractometer using a curved position-sensitive detector and a monochromatic radiation (Cu Kα, 1.5406 Å). The reducibility of NiO present in the catalysts calcined at 800 °C was studied by temperature programmed reduction (TPR). The sample (200 mg) was heated at the rate of 5 °C/min in a TPR system equipped with a TCD, from room temperature to 900 °C, under a H_2(6%)/N_2 mixture with a flow of 100 N ml/min.

Raman spectra were performed using a Jobin Yvon T64000 confocal spectrophotometer with 514.5 nm ArC ion laser as excitation source.

Transmission electron microscopy micrographs were recorded with either a Philips CM12 or CM30 microscope, LaB_6 electron source, operated at 120 and 150 kV, respectively, so that the irradiation damages are limited. Specimens for TEM were prepared by gently grinding the samples, making a sonicated suspension from the resulting powder, and depositing a droplet of the suspension onto a copper microgrid coated with a lacey carbon film.

2.3. Experimental set-up

Methane decomposition reaction was carried out in gas phase by using a thermobalance (CI Electronics Ltd., UK, model MK2) equipped with mass flow and temperature controllers. This experimental system allows continuous recording of the sample weight changes and temperature during reaction. Catalyst reduction was performed in situ at 750 °C for 2 h using a H_2(40%)/N_2 mixture, with a flow of 250 N ml/min.

Operating conditions were: catalyst weight, 100 mg; temperature, from 600 to 700 °C; total flow rate, 750 N ml/min; feed composition (%CH_4/%H_2/%N_2), from 2.5/0/97.5 to 10/10/80. Detailed descriptions of experimental conditions during catalytic tests are given elsewhere [6].

Because of their very low yield, we have not shown the behaviour of the high Cu content catalysts.

Table 1
Chemical properties of the catalysts

	%Ni	%Cu	%Mg	%Al
$NiMgAl_2O_4$ catalyst				
Nominal composition	27.06	–	11.206	24.871
Experimental composition	26.349	–	7.558	21.039
$Ni_{0.8}{\cdot}Cu_{0.2}{\cdot}MgAl_2O_4$ catalyst				
Nominal composition	28.10	7.60	14.54	16.14
Experimental composition	22.50	6.72	12.60	15.05

3. Results and discussion

3.1. Catalysts characterization

The ICP-AES data indicate that the compositions of the precursors are very close to that of the reactive mixture (Table 1).

The diffractograms of the precursors before calcination (800 °C) show a hydrotalcite-like structure with a good crystallinity (not shown here). After calcination at 800 °C, the diffractograms show the formation of aluminates, $MgAl_2O_4$ (JCPDS file no. 75-1801), $NiAl_2O_4$ (JCPDS file no. 78-1601) with spinel-like structure and crystallized NiO, CuO and MgO (Fig. 1). The specific surface areas of the mixed oxides obtained at 800 °C are 198 m^2/g for the $NiO{\cdot}MgAl_2O_4$ and 158 m^2/g for the $NiO_{0.8}{\cdot}CuO_{0.2}{\cdot}MgAl_2O_4$.

The catalysts are active in reduced state. The reducibility of the solids can be studied by TPR (temperature programmed

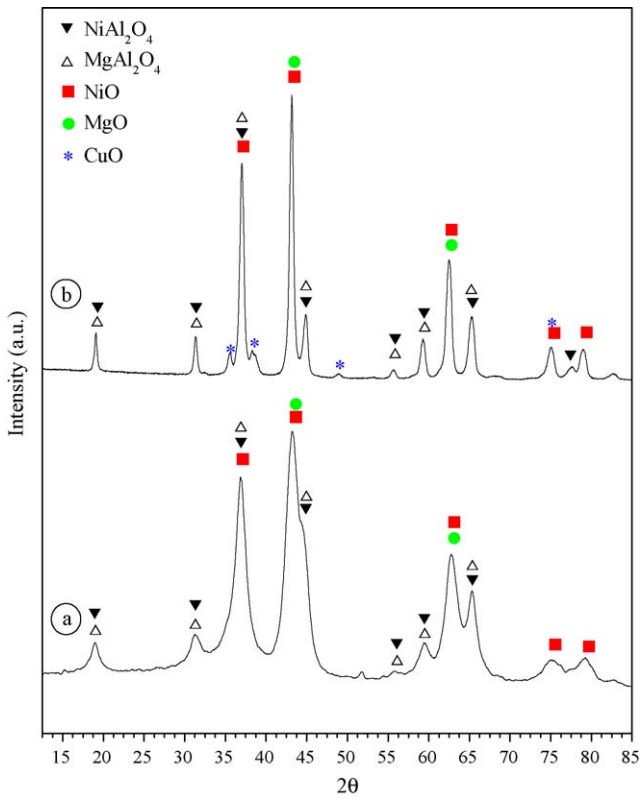

Fig. 1. X-ray diffractograms of the catalysts: (a) $Ni{\cdot}MgAl_2O_4$ and (b) $Ni_{0.8}{\cdot}Cu_{0.2}{\cdot}MgAl_2O_4$.

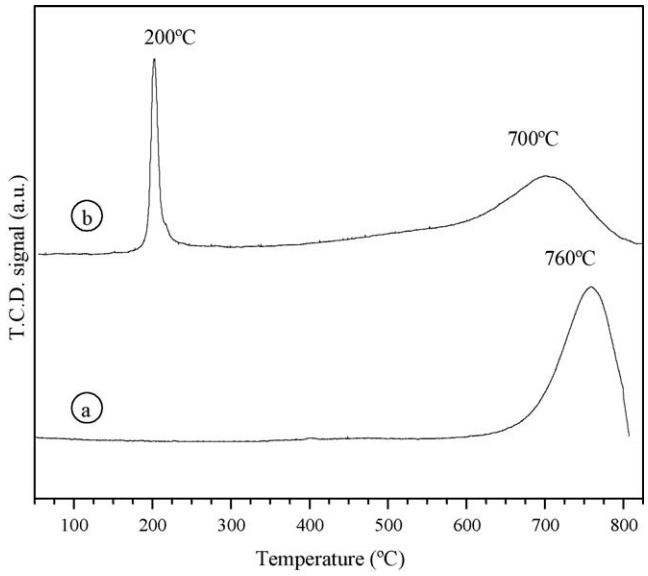

Fig. 2. Temperature programmed reduction of the catalysts: (a) Ni·$MgAl_2O_4$ and (b) $Ni_{0.8}$·$Cu_{0.2}$·$MgAl_2O_4$.

reduction) (Fig. 2). The TPR curve for the NiO·$MgAl_2O_4$ catalyst shows a main peak at around 760 °C, corresponding to the reduction of the NiO particles and the $NiAl_2O_4$ phase, since magnesium and aluminum oxides do not reduce below 900 °C. This temperature is much higher than pure black NiO. It demonstrates a strong interaction of the nickel with the neighboring metals.

The TPR profile for the $Ni_{0.8}$·$Cu_{0.2}$·$MgAl_2O_4$ catalyst shows two reduction regions. The first one, at 200 °C, corresponds to the reduction of copper ($Cu^{II} \rightarrow Cu^0$). The second region is associated with the reduction of the nickel ($Ni^{II} \rightarrow Ni^0$). The band can be decomposed into two sub-bands centered at 560 and 700 °C. The former should correspond to NiO particles in intimate contact with the support. The latter can be associated to the reduction of nickel aluminate. The Ni reduction temperature is lower for this catalyst because the Cu presence facilitates it.

These results are in accord to XRD of the samples after reaction (not shown here), where part of the nickel is in the form

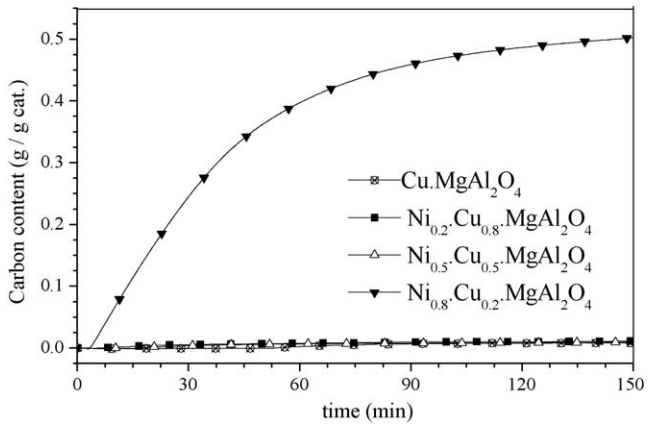

Fig. 3. Evolution with time of the carbon content for different Ni–Cu catalysts. Reaction temperature, 700 °C; feed composition, 5% CH_4/95% N_2.

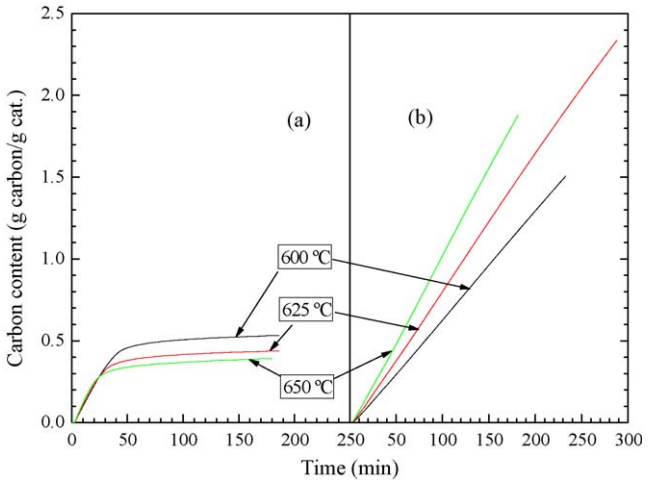

Fig. 4. Evolution of carbon concentration along time: (a) Ni·$MgAl_2O_4$ and (b) $Ni_{0.8}$·$Cu_{0.2}$·$MgAl_2O_4$.

of metallic Ni^0 and part is non-reduced Ni^{2+} species, in the form of $NiAl_2O_4$ spinel. Furthermore, a peak corresponding to graphitic carbon formed on the catalysts during the reaction appears at a 2θ equal to 26°.

3.2. Activity test

The effect of Cu addition on the carbon content is shown in Fig. 3. The operating conditions were: reaction temperature, 700 °C; feed composition, 5% CH_4/95% N_2. In Figs. 4 and 5 are the activity results obtained at three different temperatures with Ni·$MgAl_2O_4$ (a) and $Ni_{0.8}$·$Cu_{0.2}$·$MgAl_2O_4$ (b) catalysts presented. In this reaction, the measure of the evolution of the carbon content along time is a direct estimation of the catalyst activity. It can be observed for both catalysts, that the initial reaction rate increases with the reaction temperature. However, despite Ni·$MgAl_2O_4$ catalyst is initially more active than $Ni_{0.8}$·$Cu_{0.2}$·$MgAl_2O_4$ catalyst, that losses its activity almost totally after 150 min of reaction (Fig. 5a). Furthermore, the deactivation rate increases with the reaction temperature. On

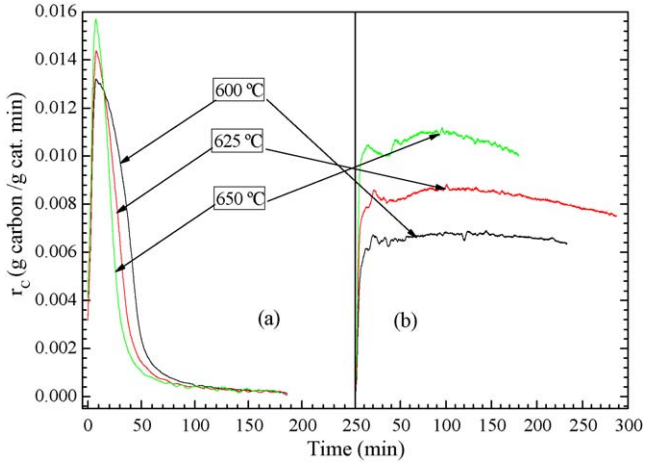

Fig. 5. Evolution of carbon formation rate along time: (a) Ni·$MgAl_2O_4$ and (b) $Ni_{0.8}$·$Cu_{0.2}$·$MgAl_2O_4$.

the other hand, the $Ni_{0.8}{\cdot}Cu_{0.2}{\cdot}MgAl_2O_4$ catalyst activity is maintained almost constant during the entire experiment (Fig. 5b). The higher resistance of this catalyst against deactivation is caused because the Cu favours a higher hydrogen mobility inhibiting the formation of encapsulating coke [5].

In agreement with the literature [5,8–10], in the case of bimetallic catalyst, the presence of Cu in concentrations of 20% (wt.% metal) has a dilution effect on the metallic phase (Cu is relatively non-catalytic), diminishing the observed reaction rate. However, it enhances both the carbon diffusion and reaction rates and thus promotes the catalytic activity when it is incorporated in small quantities. In addition, it is accepted that after the reduction step, bimetallic catalysts are able to form real alloys [9,10]. The increase in catalytic activity of bimetallic catalysts can be understood on the basis of the physicochemical properties of alloys. For instance, a decrease in melting temperature and an increase in carbon solubility are observed for alloys compared to single metals [11].

In order to have an entire vision of the positive effect of the Cu addition in the catalyst activity and stability, a complete kinetic study of the influence of operating temperatures and feed composition on the carbon content and reaction rate has been made.

3.3. Influence of reaction temperature

The effect of the reaction temperature on the carbon content and carbon formation rate is shown in Fig. 6. Feed composition in these experiments was 5% CH_4/95% N_2. Carbon formation rate curves have been calculated from the numerical derivative of the experimental carbon content versus time curves. An increase in the reaction temperature heightens in the kinetics of methane decomposition and deactivation reaction. In consequence, the carbon content shows a maximum at 660 °C. When the reaction temperature is lower, the carbon content is smaller but deactivation is not observed for the reaction time. The deactivation rate is faster at high reaction temperatures and, as a result, a reduction in the carbon content is observed. When deactivation takes place, the carbon formation rate curves show an initial period of rapid growth until a maximum is reached. This period is followed by a decrease in the carbon formation rate until a residual constant value is reached. During the period of activity decay, the deactivation rate is higher than the filament formation rate. In this reaction, the rate of carbon filament formation is in fact the reaction rate and therefore a measurement of the true catalyst activity. In most cases, the carbon formation corresponds to the deposition of coke through a secondary reaction, and the higher the coking rate is, the higher is the deactivation rate and the lower is the remaining activity.

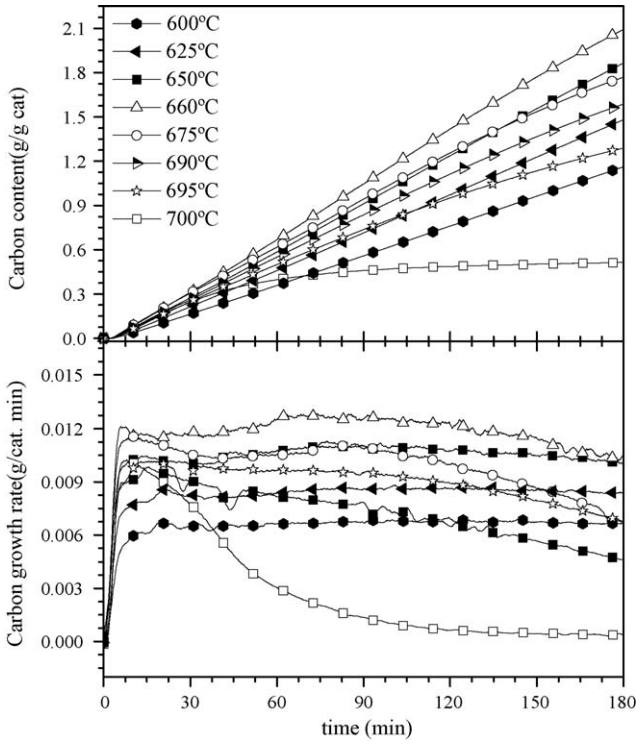

Fig. 6. Evolution with time of the carbon content (upper) and the carbon growth rate (lower). Influence of reaction temperature. Feed composition: 5% CH_4/95% N_2.

3.4. Influence of hydrogen concentration

Fig. 7 shows the effect of P_{H_2} at a constant P_{CH_4} (0.05 atm) and operating temperature (650 °C). When the P_{H_2} is 0.02 atm,

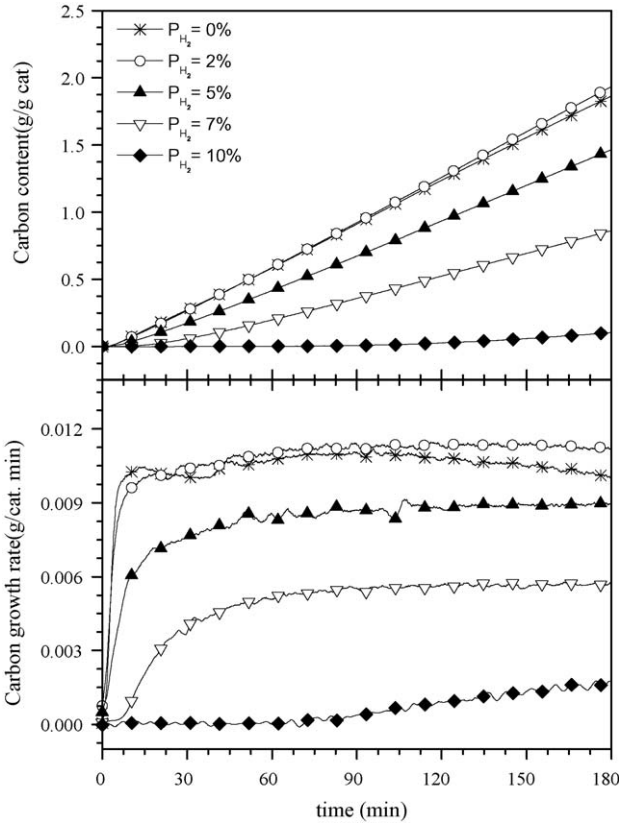

Fig. 7. Evolution with time of the carbon content (upper) and the carbon growth rate (lower). Influence of hydrogen partial pressure. Feed composition, 5% CH_4; reaction temperature, 650 °C.

a maximum carbon quantity is reached and the deactivation is avoided during the experiment (180 min). However, a larger P_{H_2} causes the opposite effect, a lower carbon production. In conclusion, a maximum in the influence of P_{H_2} over the carbon formation is observed. The position and magnitude of this maximum depends on the nature of the catalyst and the operating conditions [6]. The presence of this maximum can be explained by taking into account that, at low concentrations, hydrogen prevents the formation of encapsulating coke, and consequently the formation of carbon filaments is not hindered by this coke [12]. This fact could justify the increase in catalyst activity. However, at high P_{H_2} the competition between H_2 and CH_4 for the metallic surface sites causes the diminution of the formation of both, carbon filaments (negative effect) and encapsulating carbon species that deactivate the catalyst (positive effect) [5,6,12–15]. High hydrogen concentrations retard the formation of carbon filament but also prevent the deactivation of the catalyst. Under these conditions carbon formation rate is low (see Fig. 7).

3.5. Influence of methane concentration

Fig. 8 shows how the increase of P_{CH_4} (expressed as % of H_2) increases the catalyst carbon content and the carbon formation rate, because a higher methane concentration in the gas phase leads to a boost in the diffusion–precipitation process through the Ni crystallites. Besides, an increase in the deactivation rate is not observed for the considered reaction time. However, when the P_{CH_4} is 0.025 atm, the kinetic behaviour is different. The catalyst suffers stronger deactivation. It would be expected that the greater the concentration of methane, the greater is the rate of formation of polymeric species, which can encapsulate and deactivate the surface of the metallic crystallites [5,12–14,16,17].

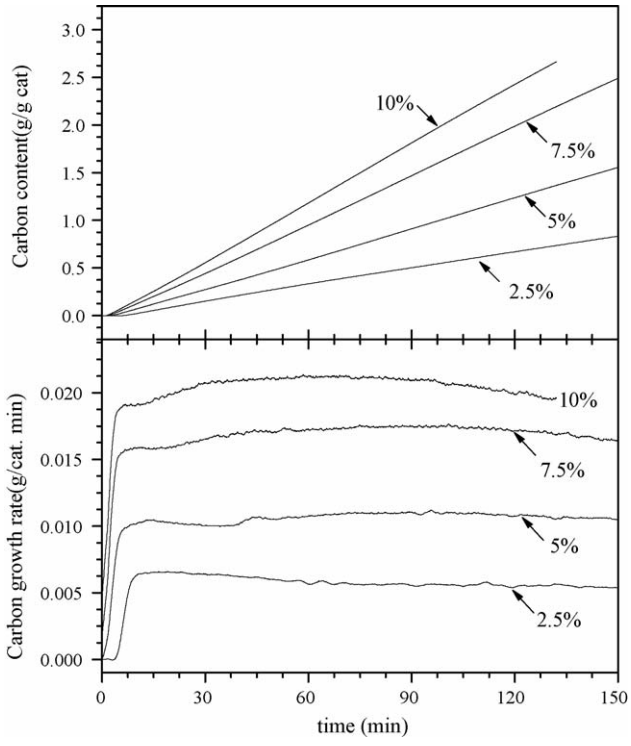

Fig. 8. Evolution with time of the carbon content (upper) and the carbon growth rate (lower). Influence of methane partial pressure (%H_2 = 0). Reaction temperature: 650 °C.

3.6. Carbon characterization

The filaments generally show a diameter in the range of 60–100 nm (with some thicker ones up to 400 nm). The graphene-based structure of the nanofilaments observed in XRD patterns is confirmed by the Raman spectra (not shown here). The frequency and intensity of the D- and G-Raman bands provide information about the crystallinity of CNFs [16]. In particular, the ratio I_D/I_G is inversely proportional to the dimension L_a, i.e. the average planar size of the perfect graphenes [19]. The values reported in Table 2 indicate that the CNFs produced on $Ni_{0.8}$·$Cu_{0.2}$MgAl have a high disordered structure (smaller L_a). The discrepancy between L_a values obtained from XRD and Raman spectroscopy comes from the underestimation of values obtained with Raman due to the dominant effect of the smallest coherent domains [18]. The large difference between the results of the two techniques for CNFs from $Ni_{0.8}$·$Cu_{0.2}$·$MgAl_2O_4$ indicates that they present a high dispersion of crystallite sizes although the average polyaromatic coherent domains are large (following both dimensions L_a and L_c).

Fig. 9a shows typical TEM images of the CNFs formed over $Ni_{0.8}$·$Cu_{0.2}$·$MgAl_2O_4$. Nanofilaments actually nanofibers (i.e. not hollowed) are frequently attached to the catalyst particle where they have grown from (Fig. 9a). The metallic Ni–Cu particle is detached from the support possibly because it is pushed up by the nanofibers during its growth [20]. Octahedral or cubo-octahedral catalyst particles of relatively large size (100–400 nm) were found well crystallized, giving rise to sharp and bright dots in electron diffraction patterns (Fig. 9b, arrows), and to lattice fringes in high-resolution TEM images (Fig. 9e). The sample appeared quite homogeneous (a very large majority of the filaments are from the same type) with only a scarce occurrence of other filament types (herringbone type, not illustrated). Fig. 9d indicates that the graphene layers are oriented parallel to the particle surface, making them perpendicular to the filament axis (‘platelet’ texture) [21]. Actually, arrows in Fig. 9a indicates the very location where the nanofilament was about to split, due to easy gliding resulting from the weak van der Waals forces between stacked

Table 2
Structural parameters of carbon nanofilaments: interlayer distance d_{002}, average size of coherently scattering domains along the normal to graphene layers (L_c) and in the graphene plane (L_a) from XRD

Catalyst	$Ni_{0.8}$·$Cu_{0.2}$·$MgAl_2O_4$
d_{002} (nm)	0.331
L_c (XRD) (nm)	8.3
L_a (XRD) (nm)	7.3
I_D/I_G (Raman)	2.4
L_a (Raman) (nm)	1.8

L_a from Raman spectra is calculated with $I_D/I_G = 4.4/L_a$ [16].

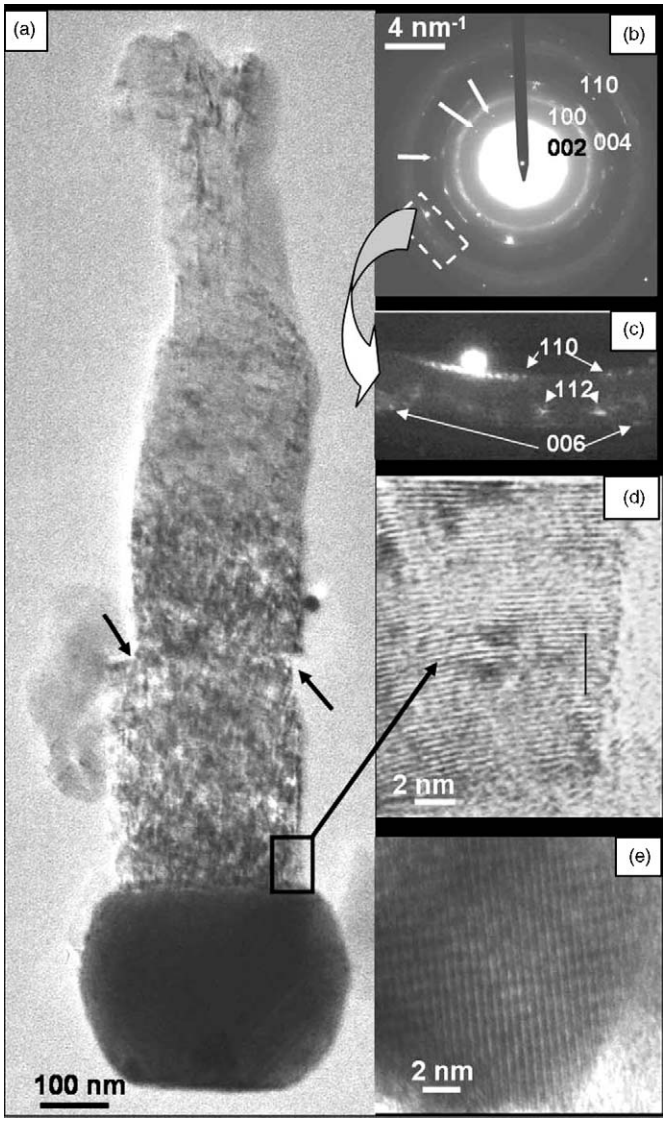

Fig. 9. TEM images of carbon nanofiber formed over $Ni_{0.8}$·$Cu_{0.2}$·$MgAl_2O_4$. (a) Low magnification. Arrows indicate steps at the CNF surface which result from a slight gliding; (b) electron diffraction pattern giving rise to the labelled rings, with a very limited contribution of catalyst particles (arrowed spots); (c) enlargement of the area framed in (b); (d) high magnification image; (e) high magnification image of catalyst particle.

graphenes. Square-like particles that make up most of the specimen after the TEM preparation procedure (grinding) are therefore merely platelet–CNF fragments (not illustrated), most of them exhibiting the same graphene display. Interestingly, such a graphene display implies that the fiber surface is actually made of free-graphene edges, meaning that high surface reactivity and surface energy are expected. As stated by numerous Bragg fringes (dark contrasts), the carbon nanofilaments decorated with the nanotexture are quite high. Electron diffraction patterns (Fig. 9b) exhibit rather sharp and dotted reflections together with multiple order reflections (e.g. 0 0 2, 0 0 4, 0 0 6) which both indicate large coherent domains, which is consistent with the high nanotexture quality. The most outstanding feature is, however, that nanofibers exhibit at least a partially graphitic structure, i.e. many of the graphene layers are stacked according to the ABAB stacking sequence typical of graphite. Such a structural feature is ascertained by the occurrence of three-indice reflections such as 1 1 0 and 1 1 2 (Fig. 9c), as opposed to two-indice asymmetric bands (such as 1 0 and 1 1) that are found in turbostratic, polyaromatic carbon materials such as regular multi-wall carbon nanotubes (MWNTs). All these results are in full agreement with the previous data, particularly the interplanar distance d_{002} measured at 0.333 nm in Fig. 9d, which matches well the 0.331 nm measured from XRD (Table 2) and is very close to that of pure graphite (0.335 nm).

It is now accepted that the syntheses of the filaments proceeds in three stages: (i) a decomposition of methane on (1 0 0) and (1 1 0) surface planes of the catalyst particle; (ii) a carbon dissolution and diffusion through the particle; (iii) a carbon segregation and precipitation on the (1 1 1) surface plane with the filament growth from this plane.

It appears that the decomposition reaction of methane and the formation of carbon filaments are structurally sensitive since the introduction of Cu changes the size and partly the shape of metal particles then involving modifications in the diameter and the texture of the carbon filaments. The platelet fibers grow up from the largest particles (which show in the present case the widest faces) which are formed with 7.6 wt.% of Cu (lower Cu content induces the formation smaller metal particles on which grow herringbone type filaments). In agreement with the literature [22,23], it seems that the copper, which has a surface energy lower than the nickel one (respectively, 1.85 and 2.45 J m^{-2}), would segregate to the surface during the reduction step and especially during the reaction time, as shown by XPS analyses (atomic ratio [Cu]/[Ni] = 0.21 before reaction and 1 after reaction). This probably induces a widening of the particle faces by minimisation of the energy, in particular at the surface of the (1 1 1) plane, which matches with (0 0 2) graphite plane.

4. Conclusions

In this work, we have studied a series of catalysts ($Ni_xCu_{1-x}MgAl$ with $0 \leq x \leq 1$) obtained by calcination of lamellar double hydroxides. The physicochemical characteristics (reducibility, particle size) of these catalysts depend on their composition. It appears that the reduced catalysts are formed by particles of Cu^0 and Ni^0 on MgO, $NiAl_2O_4$ and $MgAl_2O_4$ support.

The kinetic study of carbon growth from the catalytic decomposition of methane indicates a high activity of the catalysts at low Cu contents ($x \leq 0.2$) and a high stability along time of the catalysts $Ni_xCu_{1-x}MgAl$ compared to that of NiMgAl homologue.

The hydrogen competes with the methane for the surface sites inhibiting both the formation of carbon filaments and the formation of encapsulating coke, which deactivates the catalyst. An increase in the methane concentration leads to an increase in the rate of carbon filament formation. An increase in the operating temperature favours the formation of both carbon filaments and encapsulating coke. At high reaction

temperatures, the catalyst deactivation effect is more marked than that of the nucleation and growth of new filaments. This explains the reduction in the formed amount of carbon at high temperatures.

The carbon products are typically polyaromatic carbon nanofibers or nanotubes, with either a graphitic or a turbostratic structure depending on the texture (either 'platelet' or 'herringbone'). There is a wide distribution of catalyst particle sizes, hence a wide distribution of filament diameters (between 60 and 400 nm). The thickest filaments are nanofibers with a 'platelet' texture (graphene layers perpendicular to the fiber axis) with large domains of high nanotexture quality. On the other hand, filaments with a diameter smaller than 50 nm are nanotubes with a 'herringbone' texture, where the graphene layers are oriented obliquely, with the angle between the graphene planes and the fiber axis ranging from 30° to 60°.

Acknowledgment

The authors acknowledge financial support of MEC, Madrid, Spain (Project: CTQ 200-03973/PPQ).

References

[1] J.N. Armor, Appl. Catal. A 176 (1999) 159.
[2] M. Steinberg, H.C. Cheng, Int. J. Hydrogen Energy 14 (1989) 797.
[3] T. Zhang, M.D. Amiridis, Appl. Catal. A 167 (1998) 1161.
[4] T.V. Choudhary, C. Sivadinarayana, C.C. Chusuey, A. Klinghoffer, D.W. Goodman, J. Catal. 199 (2001) 9.
[5] Y. Li, J. Chen, L. Chang, Y. Qin, J. Catal. 178 (1998) 76.
[6] J.I. Villacampa, C. Royo, E. Romeo, A. Montoya, P. del Angel, A. Monzón, Appl. Catal. A 252 (2003) 363.
[7] N. Latorre, J.I. Villacampa, C. Royo, E. Romeo, A. Montoya, P. del Angel, A. Monzón, in: Proceedings of the 18th North American Meeting of Catalysis Society, Cancun, México, 1–6 June, 2003.
[8] I. Alstrup, J. Catal. 109 (1988) 241.
[9] E. Flahaut, A. Govindaraj, A. Peigney, Ch. Laurent, A. Rousset, C.N.R. Rao, Chem. Phys. Lett. 300 (1999) 236.
[10] K.C. Khulbe, R.S. Mann, Catal. Rev. Sci. Eng. 24 (1982) 311.
[11] A. Moisala, A.G. Nasibulin, E.I. Kauppinen, J. Phys. Condens. Matter 15 (2003) S3011.
[12] M.L. Toebes, J.H. Bitter, A.J. van Pillen, K.P. de Jong, Catal. Today 76 (2002) 33.
[13] Y. Li, J. Chen, L. Chang, Appl. Catal. A 163 (1997) 45.
[14] Y. Li, J. Chen, Y. Qin, L. Chang, Energy Fuels 14 (2000) 1188.
[15] M.C. Demichelli, E.N. Ponzi, O.A. Ferreti, A.A. Yeramian, Chem. Eng. J. 46 (1991) 129.
[16] L. Piao, Y. Li, J. Chen, L. Chang, J.Y.S. Lin, Catal. Today 74 (2002) 145.
[17] K.P. de Jong, J.W. Geus, Catal. Rev. Sci. Eng. 42 (2000) 481.
[18] T.V. Reshetenko, L.B. Avdeeva, Z.R. Ismagilov, V.V. Pushkarev, S.V. Cherepanova, A.L. Chuvilin, V.A. Likholobov, Carbon 41 (2003) 1605.
[19] D.S. Knight, W.B. White, J. Mater. Res. 4 (1989) 385.
[20] P. Serp, M. Corrias, P. Kalk, Appl. Catal. A 253 (2) (2003) 337.
[21] H. Wang, R.T.K. Baker, J. Phys. Chem. B 108 (2004) 20273.
[22] L.B. Avdeeva, O.V. Goncharova, D.I. Kochubey, V.I. Zaikovskii, L.M. Plyasova, B.N. Novgorodov, Sh.K. Shaikhutdinov, Appl. Catal. A 141 (1996) 117.
[23] T.V. Reshetenko, L.B. Avdeeva, Z.R. Ismagilov, A.L. Chuvilin, Appl. Catal. A 247 (2003) 51.